PHYSICAL REVIEW FLUIDS **8**, 123802 (2023)

Negatively buoyant vortices in the Boussinesq-Euler equations

G. G. Rooney
Met Office, FitzRoy Road, Exeter EX1 3AL, United Kingdom
and School of Mathematics, University of Leeds, Leeds LS2 9JT, United Kingdom

(Received 28 April 2023; accepted 10 October 2023; published 15 December 2023)

A previous model of a two-dimensional, stratified dipole is applied to a cylindrical vortex of dense fluid traveling across the lower boundary of a semi-infinite, unstratified ambient. The vortex is semicircular in profile. The model is derived from the Boussinesq-Euler equations and hence is an idealization neglecting the effects of viscosity, density diffusion, and friction. This is similar to other idealized models of dense fluid flow. The flow maintains a steady state through a balance of positive and negative vorticity generation as the dense fluid travels around the vortex. Numerical experiments are performed to investigate the stability and behavior of isolated and interacting vortices of this type.

DOI: 10.1103/PhysRevFluids.8.123802

I. INTRODUCTION

There are many environmental situations in which a finite volume of dense fluid spreads across a lower boundary under the action of the buoyancy force. Often, a large part of the dense fluid is initially concentrated at the spreading front, particularly at high Reynolds number [1]. Processes such as vortex generation and mixing act to diffuse the (negative) buoyancy through a larger volume of fluid behind the front, while the densest fluid tends to remain close to the front [2]. These flows may often be approximated as two-dimensional or axisymmetric, depending on the source or domain geometry. Front conditions are also often compared with idealized models of constant-flux currents [3] in the absence of similar finite-volume front models [4].

A sufficiently large volume of dense fluid such as a thunderstorm outflow [5] may travel a considerable distance and yet retain a high Reynolds number. Being no longer fed by any source, it is similar in some respects to a solitary wave, transporting dense fluid. In this context, one starting point for the further development of finite-volume models may be the work of [6] on stratified dipoles with horizontal axes of vorticity, propagating horizontally through an homogeneous environment. Yih's dipoles have received little attention in the past 50 years, although they bear mathematical similarity to other solitary-wave structures such as atmospheric "modons" [7], in which the vortical axes are vertical. The stratified dipole may also be viewed as an extension of the uniform-density Chaplygin-Lamb dipole [8,9]. Structures of the latter type have been produced experimentally, e.g., by [10].

The model of [6] and related work are described here in Sec. II. Following this, reinterpretation of the theory as describing a steady, negatively buoyant vortex in contact with a lower boundary (somewhat like a solitary wave) is given in Sec. III. This forms the basis for numerical experiments investigating the behavior and interactions of such vortices, set out in Secs. IV and V.

II. PREVIOUS WORK

A. Two-dimensional flow

The Boussinesq-Euler equations for flow velocity $\mathbf{u}$ and positive pressure and density perturbations p', ρ' from a reference state of hydrostatic equilibrium $\nabla p_0 = \rho_0 \mathbf{g}$

are [11]

$$\frac{D\mathbf{u}}{Dt} = -\left(\frac{1}{\rho_0}\right)\nabla p' + \frac{\rho'}{\rho_0}\mathbf{g}, \tag{1}$$

where $\mathbf{g} = -g\mathbf{k}$ is the acceleration due to gravity (taking the vertical direction to be aligned with the z coordinate) and p_0 and ρ_0 are the background pressure and density, respectively.

Letting $g' = g\rho'/\rho_0$ denote the reduced gravity, then (1) becomes

$$\frac{D\mathbf{u}}{Dt} = -\left(\frac{1}{\rho_0}\right)\nabla p' - g'\mathbf{k}. \tag{2}$$

The curl of (1) yields the corresponding vorticity equation

$$\frac{D\boldsymbol{\omega}}{Dt} = \boldsymbol{\omega} \cdot \nabla\mathbf{u} - \nabla g' \times \mathbf{k}. \tag{3}$$

Thus the vertical orientation of $\mathbf{g}$ means that horizontal density gradients generate vorticity, also horizontal.

Assuming the fluid to be incompressible, although not necessarily homogeneous in density, then

$$\nabla \cdot \mathbf{u} = 0. \tag{4}$$

If the flow is further assumed two-dimensional in the x-z plane, then the respective u and w velocity components are given by the stream function ψ,

$$u = \frac{\partial \psi}{\partial z}, \quad w = -\frac{\partial \psi}{\partial x}, \tag{5}$$

and

$$\boldsymbol{\omega} = \nabla \times \mathbf{u} = \mathbf{j}\,\nabla^2_{xz}\,\psi, \tag{6}$$

where ∇^2_{xz} is the Laplacian in the x-z plane. Only the y component of vorticity, which may be denoted ω, remains, thus $\boldsymbol{\omega} \cdot \nabla\mathbf{u} = 0$. Also

$$-\nabla g' \times \mathbf{k} = \mathbf{j}\,\frac{\partial g'}{\partial x} \tag{7}$$

and

$$\mathbf{u} \cdot \nabla\boldsymbol{\omega} = \mathbf{j}\left(\frac{\partial \psi}{\partial z}\frac{\partial \omega}{\partial x} - \frac{\partial \psi}{\partial x}\frac{\partial \omega}{\partial z}\right). \tag{8}$$

For steady two-dimensional flow, (7) and (8) are then the only nonzero terms in (3), which then becomes

$$\frac{\partial \psi}{\partial z}\frac{\partial \omega}{\partial x} - \frac{\partial \psi}{\partial x}\frac{\partial \omega}{\partial z} - \frac{\partial g'}{\partial x} = 0. \tag{9}$$

The divergence of the steady-state form of (2) produces Poisson's equation for the pressure,

$$\frac{1}{\rho_0}\nabla^2 p' = -\nabla \cdot (\mathbf{u} \cdot \nabla\mathbf{u}) - \frac{\partial g'}{\partial z}, \tag{10}$$

for which the solution of (9) provides the source terms. Moreover it can be shown that, for an incompressible fluid, the nonlinear term in (10) contains only first derivatives of the velocity components; see, for example, [12]. Thus, for continuous velocity and density fields, it may be expected that the pressure and its first derivative are continuous.

B. Dipole in a homogeneous fluid

If the fluid has uniform density, then the quantity in (8) must equal zero. This can occur in regions of the flow where $\omega = 0$, i.e., irrotational flow. Then the continuity equation and the resulting stream function define the flow. Another analytically tractable situation for fluid of uniform density is when

$$\omega \propto \psi. \tag{11}$$

Then (8) is null as required and, from (6), the stream function must satisfy

$$\nabla_{xz}^2 \psi = -k^2 \psi, \tag{12}$$

where $-k^2$ is the proportionality constant. This equation defines the interior of the well-known Chaplygin-Lamb (CL) dipole. The exterior flow is irrotational.

The stream function of the CL dipole in the x-z plane is given in the corresponding polar coordinates (r, θ) by

$$\psi = \begin{cases} U_0\, a\, (\bar{r} - \bar{r}^{\,-1}) \sin\theta & (r > a) \\ \frac{2U_0\, a}{b\, J_0(b)} J_1(b\bar{r}) \sin\theta & (r \leqslant a) \end{cases} \tag{13}$$

(see [9] and references therein), where $x = r\cos\theta$, $z = r\sin\theta$, a is the radius of the dipole (centered on the origin), $\bar{r} = r/a$, U_0 is the uniform flow speed at infinity, J_n denotes the Bessel function of the first kind of order n, and $ka = b \approx 3.8317$ is the smallest positive root of J_1, i.e., $J_1(b) = 0$. The dipole is bounded by a circular streamline at $r = a$, where $\psi = 0$. There is also a streamline at $z = 0$. (For properties of Bessel functions see [13], for example.)

The flow in the region $r > a$ is the same as that of irrotational flow around a circle or cylinder of radius a. The choice of the dimensional constant U_0 specifies the scale of the free-stream flow at infinity, to which the dipole solution is matched. Reference [14] found a strong similarity between the structure of the CL dipole and that of a vortex dipole produced by a localized impulse in a stably stratified fluid. This was confined by the ambient stratification to a thin horizontal layer, within which the motions were approximately two-dimensional [15].

C. Yih's equation for stratified dipoles

Conservation of density following fluid particles implies that $\rho' = \rho'(\psi)$, for instance,

$$g' = \sigma \left(\frac{g}{a^3}\right)^{1/2} \psi, \tag{14}$$

where σ is a dimensionless constant, with a sign to be determined later. This means diffusion of density is neglected and is equivalent to the case of constant $\mathrm{d}\rho'/\mathrm{d}\psi$. Then (3) becomes

$$\frac{\partial \psi}{\partial z}\frac{\partial \omega'}{\partial x} - \frac{\partial \psi}{\partial x}\frac{\partial \omega'}{\partial z} = 0, \tag{15}$$

where

$$\omega' = \omega + \sigma \left(\frac{g}{a^3}\right)^{1/2} z. \tag{16}$$

Similarly to the homogeneous case, (15) would be satisfied if

$$\omega' = -m^2 \psi, \tag{17}$$

where m, like k, is an unknown constant with units of inverse length. Then using (6),

$$\nabla_{xz}^2 \psi + \sigma \left(\frac{g}{a^3}\right)^{1/2} z = -m^2 \psi, \tag{18}$$

which is the Boussinesq equivalent to the equation of [6], previously derived by [16]. The derivation of [16] did not go via the vorticity equation as above; however, this method highlights the link to the CL dipole in a uniform-density fluid.

Reference [6] considered solutions of (18) within the circle $r = a$, with $\psi = 0$ on the boundary. These are

$$\psi = \begin{cases} \sigma \frac{(ga^3)^{1/2}}{8} (\bar{r} - \bar{r}^3) \sin\theta & (m = 0) \\ \sigma \frac{(ga^3)^{1/2}}{h^2} \left(\frac{J_1(h\bar{r})}{J_1(h)} - \bar{r} \right) \sin\theta & (m > 0) \end{cases}, \tag{19}$$

where $h = ma$ and so is dimensionless. Assuming the exterior of the circle consists of homogeneous fluid, then the flow there is governed by $\nabla^2_{xz}\psi = 0$, so that the solution for $r > a$ is the same as the external flow around the CL dipole (13).

The corresponding reduced gravity may be obtained from (14), and the vorticity from (16) and (17). Thus

$$g' = \frac{\sigma^2 g}{8} (\bar{r} - \bar{r}^3) \sin\theta, \quad \omega = -\sigma \left(\frac{g}{a} \right)^{1/2} \bar{r} \sin\theta \quad (m = 0), \tag{20a}$$

$$g' = \frac{\sigma^2 g}{h^2} \left(\frac{J_1(h\bar{r})}{J_1(h)} - \bar{r} \right) \sin\theta, \quad \omega = -\sigma \left(\frac{g}{a} \right)^{1/2} \frac{J_1(h\bar{r})}{J_1(h)} \sin\theta \quad (m > 0). \tag{20b}$$

The equivalent dimensionless fields are given by $\psi/(ga^3)^{1/2}$, g'/g, and $\omega/(g/a)^{1/2}$.

D. Modons

Around the same time as the work of [6], [17] and [18] considered a similar equation to (18) for flow in a "midlatitude β plane" i.e., approximating fluid motion at midlatitudes on the surface of a rotating planet via a truncated expansion of the Coriolis parameter [19]. This produces a latitude-dependent term in the stream function equation (the "β term"), equivalent mathematically to that proportional to z in (18).

Similar solutions with a circular bounding streamline to those above were obtained, representing solitary Rossby waves, also known as "modons." In [17], for instance, the equation for the stream function, and the resulting vorticity, are essentially the same as the expressions in the previous subsection but with the parameter β replacing $\sigma(g/a^3)^{1/2}$. Unlike the buoyant-flow case however, the β term is also present in the equation governing the exterior flow, which is consequentially different from that of the CL dipole [18]. Further discussion of modons is given by [20] or [7], for instance.

III. APPLICATION OF THE SOLUTIONS TO DENSE-FLUID FLOWS

A. Lower boundary at $z = 0$

Reference [6] envisaged (19) as representing a stratified, cylindrical dipole with a circular bounding streamline moving horizontally in an unstratified background, the upper and lower halves of the dipole having opposite-signed density perturbations.

It may be seen that the formulas for g' are functions of σ^2 rather than σ. Thus the sign of ψ depends on the sign of σ, but that of g' does not. If the functions of $\bar{r}$ in (19) remain positive over $0 < \bar{r} < 1$, then the density perturbation in the upper half of the dipole ($z \geqslant 0$) is positive. This may be interpreted as the propagation of a half-cylinder of denser fluid along the free-slip lower boundary of an otherwise homogeneous environment. The sign of σ will determine the sense of vortex rotation via ψ, which may be identified with the direction of travel.

As a buoyant fluid element travels around the vortex, the horizontal buoyancy gradient creates vorticity as it travels upward in the "leading" part. The opposite buoyancy gradient then creates vorticity of the opposite sign, effectively reducing the total, as it travels symmetrically down the “trailing” part. Thus the buoyancy and vorticity fields may represent a time-independent, balanced state.

Given the Boussinesq assumption, it is also appropriate to restrict the solutions to those for which $(g'/g) \ll 1$. This may be achieved through control of the magnitude of σ, provided h is not sufficiently close to a root of $J_1(h)$ so that $J_1(h) \to 0$.

B. Speed of translation

Starting from (1) it may be shown using the method of [16] that the streamline Bernoulli constant for these equations is

$$H = \left(\frac{p'}{\rho_0} + \frac{1}{2}\mathbf{u}\cdot\mathbf{u}\right) + \frac{g\rho' z}{\rho_0}. \tag{21}$$

Since $\rho' \to 0$ at the boundary of the vortex, the tangential velocity is chosen to match that of the exterior flow. This is also the boundary condition of [6].

The polar equivalents of (5) are

$$u_r = \frac{1}{r}\frac{\partial\psi}{\partial\theta}, \quad u_\theta = -\frac{\partial\psi}{\partial r}, \tag{22}$$

and hence at $\bar{r} = 1$, $u_\theta = -2U\sin\theta$, where

$$U = \begin{cases} -\sigma\frac{(ga)^{1/2}}{8} & (m=0) \\ -\sigma\frac{(ga)^{1/2}}{2h^2}\left(2 - \frac{hJ_0(h)}{J_1(h)}\right) & (m>0) \end{cases}. \tag{23}$$

As with the CL dipole, the exterior flow in $\bar{r} > 1$ is then given by

$$\psi = Ua(\bar{r} - \bar{r}^{-1})\sin\theta, \tag{24}$$

so that the values of U given by (23) then specify the free-stream flow speed at infinity. To give one value which will be relevant to the numerical comparison in later sections, at $h = 2$, $U/(ga)^{1/2} \approx -0.153\,\sigma$.

The mean reduced gravity of the semicircular vortex (with area $\pi a^2/2$) is given by

$$g'_M = \left(\frac{2}{\pi}\right)\int_{\theta=0}^{\theta=\pi}\int_{\bar{r}=0}^{\bar{r}=1} \bar{r}g'\,\mathrm{d}\bar{r}\,\mathrm{d}\theta = \begin{cases} \frac{\sigma^2 g}{15\pi} & (m=0) \\ \frac{4\sigma^2 g}{\pi h^2}I(h) & (m>0) \end{cases}, \tag{25}$$

where

$$I(h) = \int_0^1 \left(\frac{\bar{r}J_1(h\bar{r})}{J_1(h)} - \bar{r}^2\right)\mathrm{d}\bar{r}. \tag{26}$$

Using this and the free-stream flow speed $|U|$, the bulk Froude number is then

$$\mathrm{Fr} = \frac{|U|}{(ag'_M)^{1/2}} = \begin{cases} \frac{\sqrt{15\pi}}{8} \approx 0.858 & (m=0) \\ \sqrt{\frac{\pi}{I(h)}}\left(\frac{1}{2h} - \frac{J_0(h)}{4J_1(h)}\right) & (m>0) \end{cases}. \tag{27}$$

Figure 1 plots Fr for $m = 0$ and for $m > 0$, $0.5 < h < 3.5$, with $I(h)$ evaluated numerically. The values lie within the range 0.8–1.4. A value of order one would be expected for a gravity-driven flow of this nature at high Reynolds number.

C. Features of the solution for $m > 0$

The function of $\bar{r}$ in the expression (20b) for g' is entirely non-negative for values of h between zero and the first root of J_1, i.e., $0 < h < 3.83$.. Figure 2 shows that the radial distribution of g' does

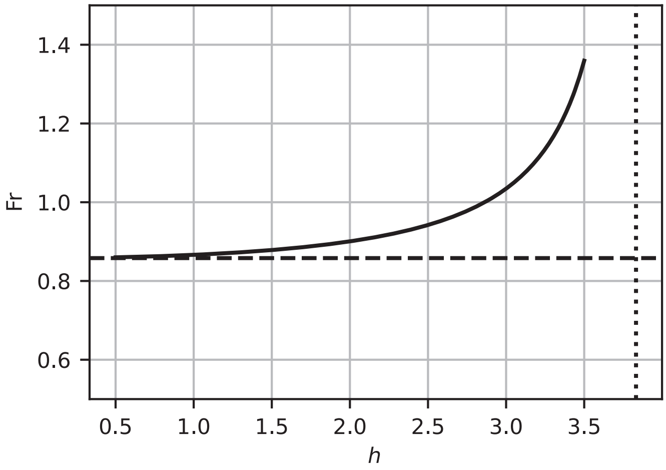

FIG. 1. Froude number (27) based on the mean reduced gravity. The horizontal dashed line indicates the $m = 0$ value, and the solid line shows the variation of the $m > 0$ value with h. The vertical dotted line marks the first root of $J_1(h)$ after $h = 0$.

not vary greatly over most of this range of h, whereas that of ω does. The normalized distributions shown for $h = 0.5$ are close to the equivalents in the case of $m = 0$.

Figure 3 shows examples of the dimensionless stream function, reduced gravity, and vorticity for the case $h = 2$ and $\sigma = 1$.

Figure 4 shows a scatterplot of $|\bar{\omega}|$ against $|\bar{\psi}|$ calculated over a grid of points within the vortex, for the same values of h as in Fig. 2. The plotted quantities are taken from the frame in which the vortex is stationary. This is depicted in Fig. 3, in which it may also be seen that a stream

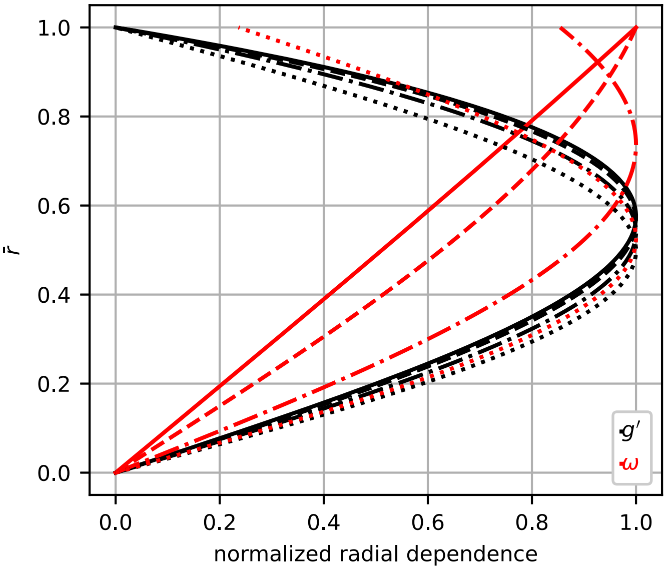

FIG. 2. Normalized distribution (the distribution divided by its peak value) of the radial functions for g' (black) and ω (red) at different values of h: 0.5 (solid), 1.5 (dashed), 2.5 (dash-dot), 3.5 (dotted).

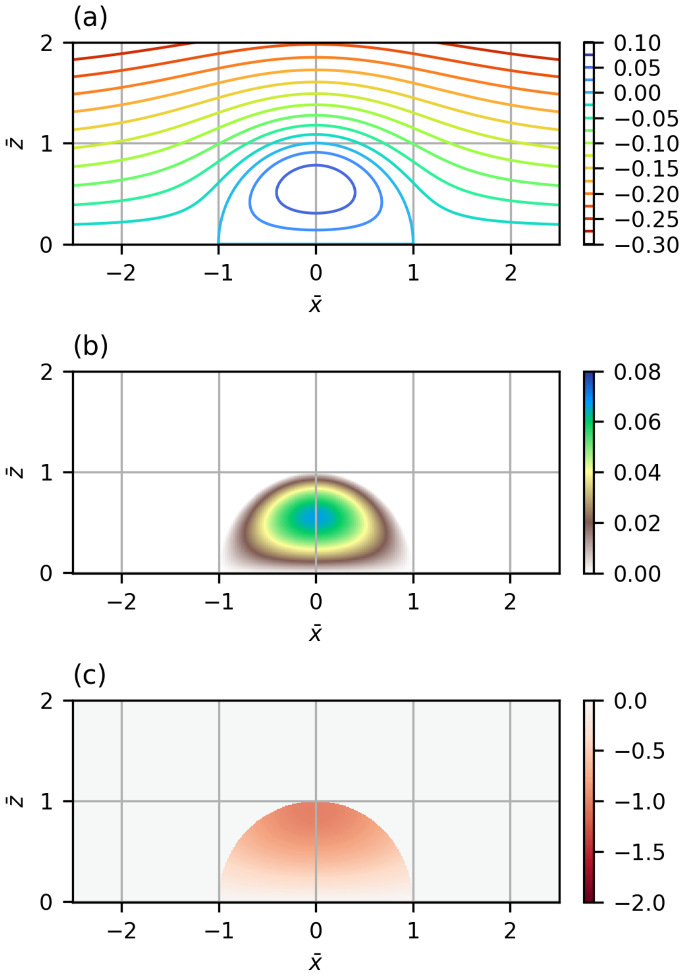

FIG. 3. Dimensionless stream function (a), reduced gravity (b), and vorticity (c) for the $m > 0$ solution with $h = 2$ and $\sigma = 1$; see Eqs. (19) and (20).

function contour within the vortex will pass through points with different magnitudes of vorticity. This is because the presence of buoyancy means that the relationship between ω and ψ is no longer 1:1. However, Fig. 4 shows that the relationship becomes (relatively) much more correlated as h approaches its limiting value. The significance of this will be discussed in Sec. VI A.

IV. NUMERICAL MODELING

A. Hydra

The fluid model Hydra [21] was used to investigate the stability and interaction behavior of these negatively buoyant vortices.

Hydra is a numerical model for simulation of two-dimensional (vertical and horizontal) flows with density inhomogeneities. It solves the Boussinesq-Euler equations by the combined Lagrangian advection method (CLAM) [22]. This aims to minimize numerical diffusion by combining a pseudospectral method at larger scales and contour advection [23] at smaller scales. The reduction of diffusion assists with density conservation following fluid particles. Hydra was previously used in [24] to investigate collisions of gravity currents. This modeling approach was also used in [25] to

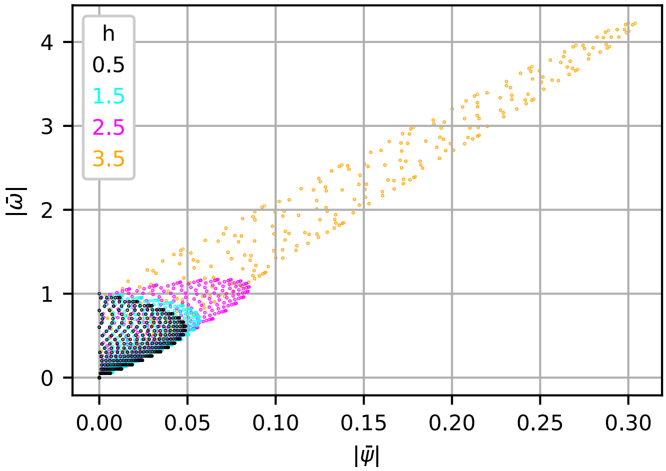

FIG. 4. Absolute, dimensionless values of vorticity and stream function, plotted against each other for different values of h as shown. These are colocated values taken from a grid of points covering the vortex.

study the contrasting case of an homogeneous solitary wave in a stratified background. References [26,27] show further examples of the methodology.

For the present problem, Hydra is used to solve the unsteady, two-dimensional system of equations

$$\frac{D\bar{\omega}}{D\bar{t}} = \frac{\partial \bar{g}'}{\partial \bar{x}}, \tag{28a}$$

$$\frac{D\bar{g}'}{D\bar{t}} = 0, \tag{28b}$$

$$\nabla \cdot \bar{\mathbf{u}} = 0. \tag{28c}$$

Again, overbars denote dimensionless variables, nondimensionalized using g and a.

B. Model domain and initialization

The vortex solution (19) has a dimensionless radius of 1. For the main set of experiments, the domains were as follows. For a single vortex, the model was run on a domain of dimensionless width 6 and height 3. The streamline pattern in Fig. 3(a) suggests that these may be close to the minimum dimensions to admit approximately horizontal flow at the boundary. For vortex interactions, the domain was of width 12 and height 3. The domain is periodic in the x direction and has a free-slip surface at the upper and lower boundaries. The resolution was 256 points per three units of dimension, i.e., the smaller domain was 512 by 256 points, and the larger was 1024 by 256 points.

Two additional single-vortex experiments were performed, one with the same 6 × 3 domain but with 512 points per three units of dimension i.e., double the resolution, and one with the usual resolution of 256 points per three units of dimension but on a 12 × 6 domain i.e., double the size. These were to further examine the numerical and flow behaviors, respectively.

The model is initialized by providing fields of dimensionless reduced gravity and vorticity. There is no requirement or mechanism to initialize the velocity field. The analytical model above specifies the vortex fields in (20), and also zero buoyancy and vorticity outside the rotational region. (The fields of ω and g' in Hydra have the opposite sign conventions to the ones used here.)

All but one of the vortices in these experiments have parameter values of $h = 2$, with various values of σ as given below.

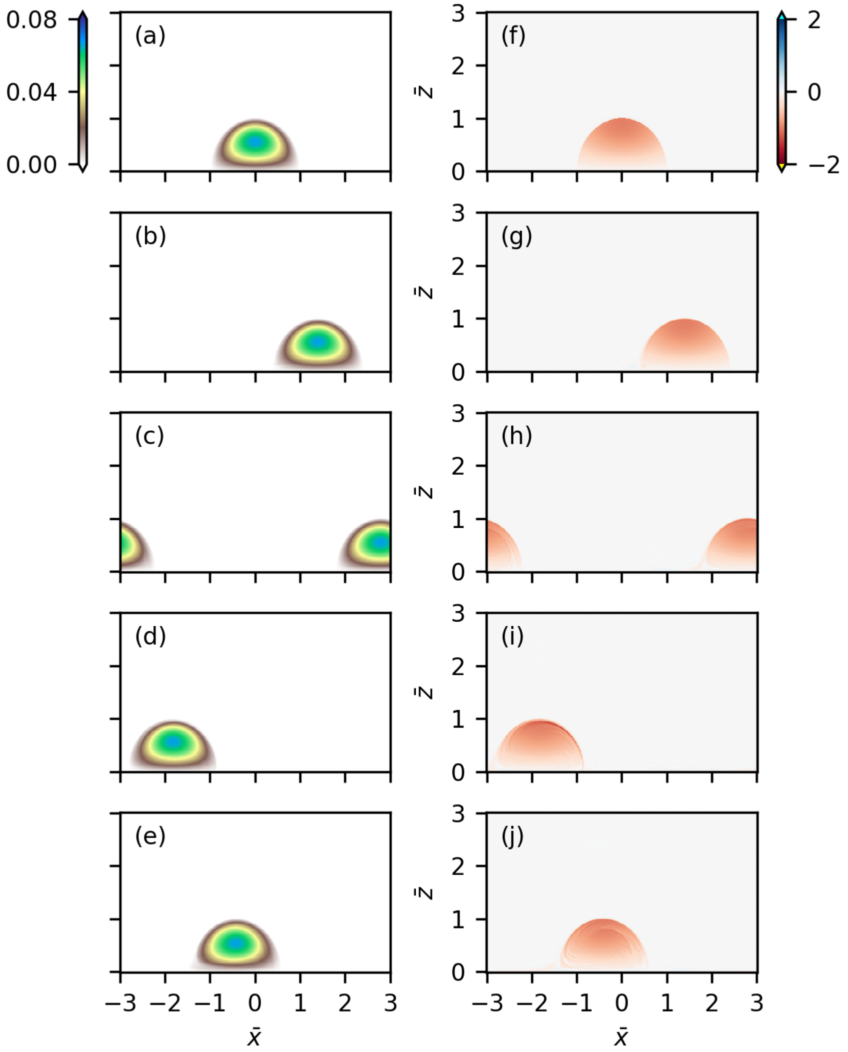

FIG. 5. Plots of the single vortex at intervals $\Delta\bar{t} = 10$ for $0 \leqslant \bar{t} \leqslant 40$. Panels (a)–(e) show the dimensionless reduced gravity, and (f)–(j) show the dimensionless vorticity. The vortex is initially centered at $\bar{x} = 0$ in the top row of panels, and time increases downwards.

V. RESULTS

Hydra was used to investigate a single vortex, and vortex interactions. Animations of the numerical experiments on vortex interactions are provided in the Supplemental Material [28].

A. Single vortex

The model was initialized on the small domain with a single vortex with parameters $h = 2$, $\sigma = 1$, and allowed to run over $0 \leqslant \bar{t} \leqslant 40$.

Plots of the dimensionless reduced-gravity and vorticity fields at dimensionless time intervals of 10 are shown in Fig. 5. Initialization via these fields does not allow for the imposition of a background (irrotational) uniform flow, hence the vortex moves left to right through the periodic domain. It maintains its internal fields relatively unchanged throughout.

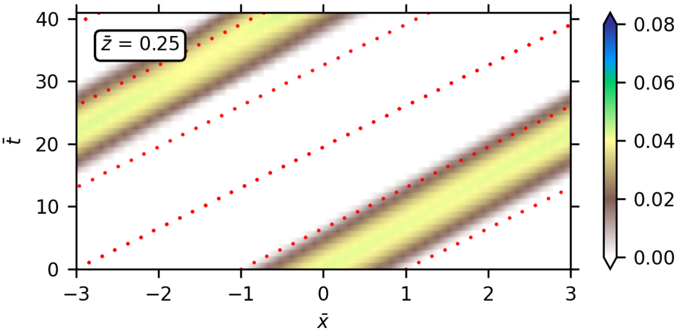

FIG. 6. Hovmöller diagram of the single vortex, plotting time against cross sections of dimensionless reduced gravity taken at height $\bar{z} = 0.25$. The red dotted lines indicate the theoretical vortex speed in an unbounded domain.

Cross sections of the dimensionless reduced gravity at a height $\bar{z} = 0.25$ are plotted as a Hovmöller diagram in Fig. 6. Also plotted is a set of lines indicating the theoretical vortex speed in an unbounded domain. For $h = 2$, the magnitude of dimensionless speed is approximately 0.153σ, as indicated in Sec. III B. This figure shows that the vortex travels slightly slower than this speed because of the domain restrictions. It also shows evidence of a small oscillation, in the fluctuating intensity of the center of the vortex swath at later times.

Figures 7 and 8 show further single-vortex experiments with the same initialization but doubled resolution or domain size, respectively. Figure 7 is essentially identical to the original experiment, indicating that the original has sufficient resolution to be deemed converged. The speed of the vortex in Fig. 8 is closer to the theoretical prediction for an unbounded domain (compare, for instance, the theoretical line at the trailing edge of the vortex). This appears to confirm that the speed is affected by the restricted domain.

B. Single, unbalanced vortex

To demonstrate how the stability of the vortex depends on the balance between the fields, the single-vortex experiment was repeated but instead of having $h = 2$ for both fields, the g' field was initialized using (20) with $h = 2.5$, $\sigma = 1$, and the ω field was initialized using (20) with $h = 1.5$, $\sigma = 1$. It should be emphasized that the same value of h for each field is required for a steady-state solution. By initializing with different values, the initial fields are deliberately perturbed away from a state of mutual balance.

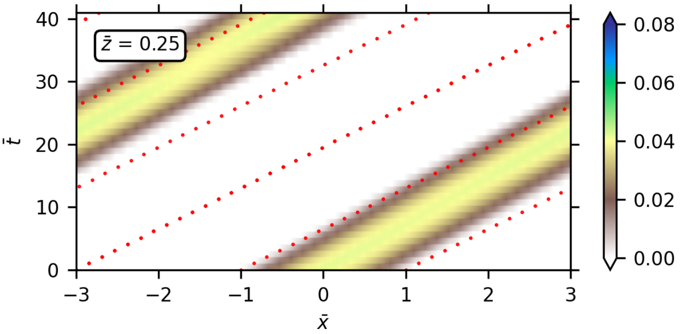

FIG. 7. Hovmöller diagram of the single vortex with doubled domain resolution compared to that in Fig. 6.

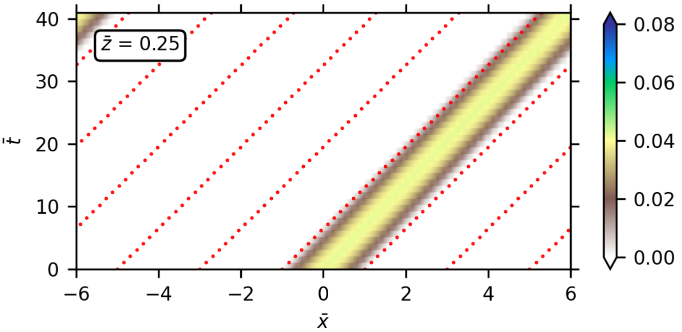

FIG. 8. Hovmöller diagram of the single vortex with doubled domain size compared to that in Fig. 6.

Plots of the dimensionless reduced-gravity and vorticity fields at dimensionless time intervals of 10 are shown in Fig. 9. It can be seen that the vorticity is no longer sufficient to maintain the equilibrium of the reduced-gravity field, and the vortex breaks down into an unsteady gravity current.

It may be remarked that the vorticity field here is still strong enough to initiate a current which travels left to right. At a greater imbalance in which g' is dominant, the initial distribution will divide into two currents traveling in opposite directions. If ω dominates, the vortex is less susceptible to breakdown, since the action of buoyancy is then relatively weak.

C. Colliding vortices

The stability of the single (balanced) vortex, even on a bounded domain, prompts a further investigation of vortex interactions to see if these solitary-wave structures are in any way robust to head-on or chasing encounters. These are described here and in the following subsection.

Two vortices were initialized at positions $\bar{x} = \pm 3$ in a domain of horizontal extent $-6 \leqslant \bar{x} \leqslant 6$. These were specified by parameters of $h = 2$ for both, and $\sigma = 1$ at $\bar{x} = -3$, $\sigma = -0.8$ at $\bar{x} = 3$. Thus they may be expected to collide near the center of the domain. The evolution of this experiment over $0 \leqslant \bar{t} \leqslant 60$ is shown in Fig. 10.

The vorticity plots indicate that the vortices may be said to touch at or shortly after $\bar{t} = 20$. Since the vorticity is discontinuous at the vortex boundaries, the touching of the vortices is more evident here than in the reduced-gravity fields. At this point the interface is quite close to vertical, although it inclines further as the collision progresses. The initial (right-to-left) buoyancy ratio is equal to the ratio of σ^2 i.e., 0.64. The study of [24] would predict from this an interface angle of around $10^\circ \pm 5^\circ$ to the vertical soon after collision, albeit for colliding gravity currents of quite a different structure. That estimate is similarly close to vertical.

The vortices do not maintain their initial shapes after collision, instead generating much small-scale structure as the fields are forced out of balance. Nonetheless the Hovmöller diagram, Fig. 11, shows a front-position evolution similar to that of nonlinear wave interaction. Rather than rebounding, the structures display some signs of emerging on the other side of the collision zone to that from which they came, despite the exchange of some buoyant fluid in the process. The postcollision fronts have speeds similar to those prior to collision, but there is a time delay for both fronts compared to their initial trajectories. This behavior is also like that observed in [24].

The approximate maintenance of the front speeds perhaps suggests that the patches or clumps of negatively buoyant fluid evident in Fig. 10(g) may still produce a bulk effect similar to the precollision, smooth distributions. Quantitatively, at the end of the experiment the ratio of total buoyancies in the lower left to lower right quadrants, which between them contain 96% of the total buoyancy, is 0.67.

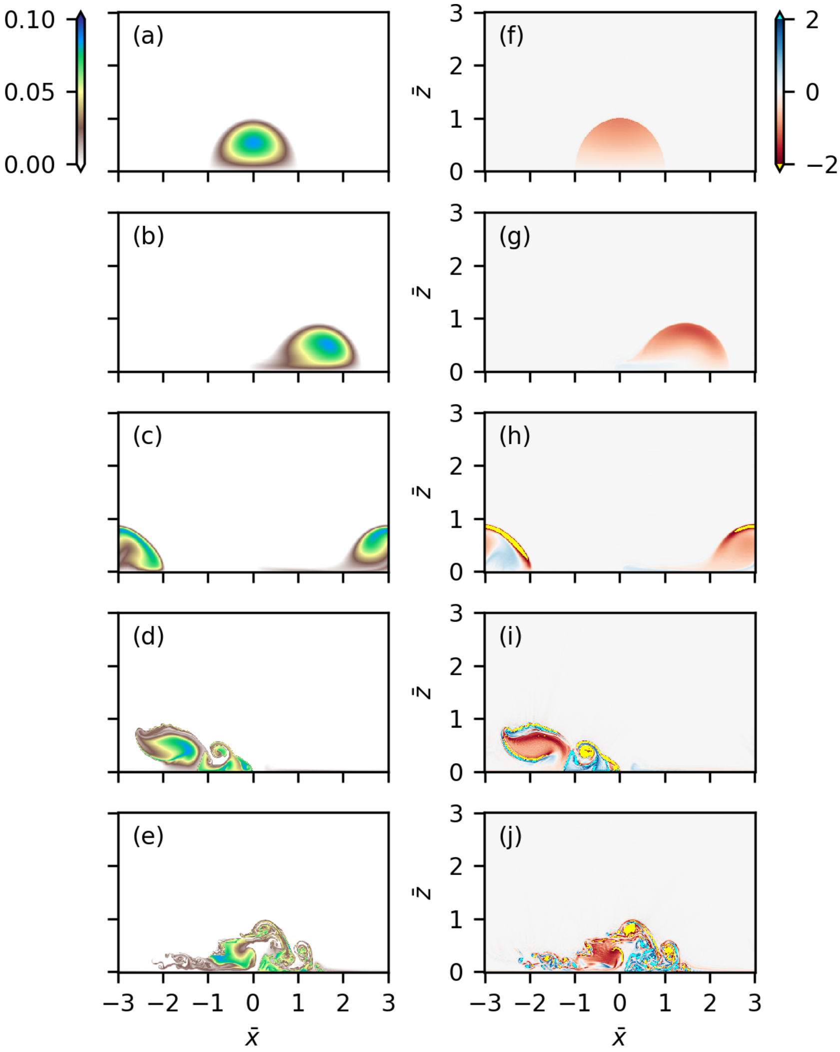

FIG. 9. Plots of the single, unbalanced vortex at intervals $\Delta\bar{t} = 10$ for $0 \leqslant \bar{t} \leqslant 40$. Panels (a)–(e) show the dimensionless reduced gravity, and (f)–(j) show the dimensionless vorticity. The vortex is initially centered at $\bar{x} = 0$ in the top row of panels, and time increases downwards.

D. Chasing vortices

A further experiment was carried out with the same domain and initial vortex positions as in the colliding experiment, described in the previous subsection. The aim this time was to analyze the interaction of vortices traveling in the same direction. They were again specified by parameters of $h = 2$ for both, and $\sigma = 1$ at $\bar{x} = -3$, $\sigma = 0.5$ at $\bar{x} = 3$. The latter vortex therefore has the same travel direction, which depends on the sign of σ, but a slower speed than the former. The pursuit takes longer to execute than a collision, hence this experiment was run over $0 \leqslant \bar{t} \leqslant 120$. The evolution of the fields is is shown in Fig. 12, noting that the time interval between frames is now $\Delta\bar{t} = 20$.

It can be seen that the stronger vortex again undercuts the weaker, and they do not recover their original structures after the encounter. Analyzing the final frame, Fig. 12(g), the divide between the patches of buoyancy appears to be at $\bar{x} \approx 1$. The ratio of the total buoyancy in the region

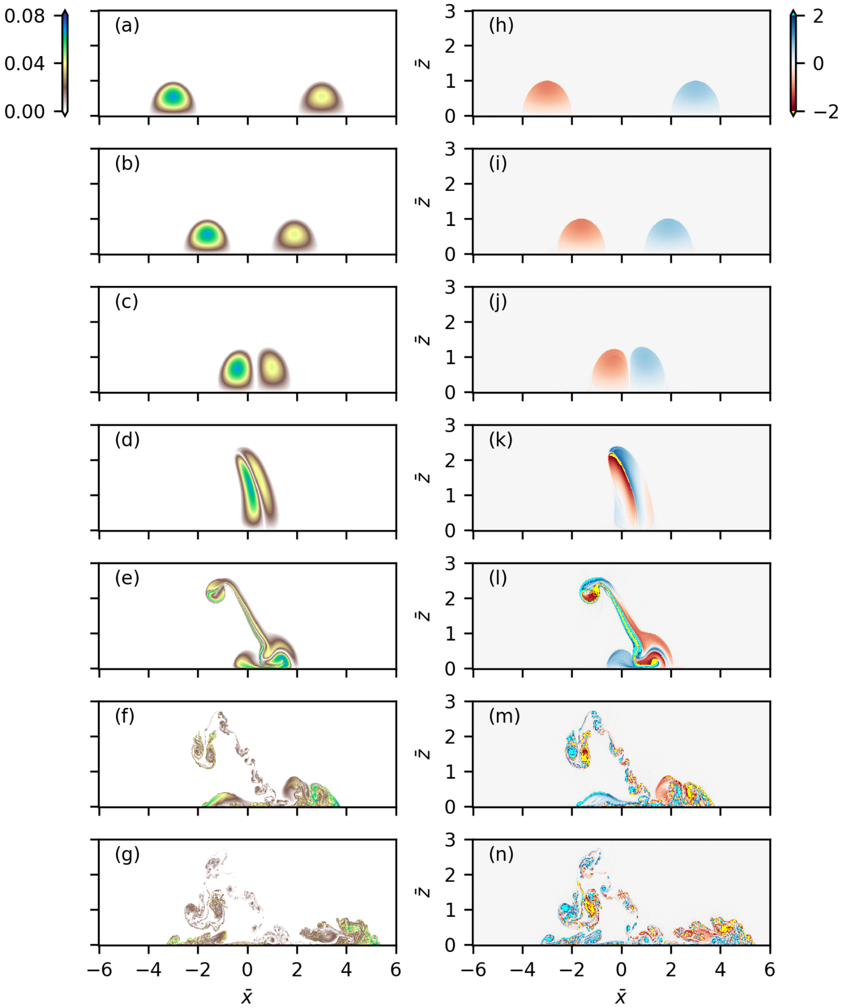

FIG. 10. Plots of the colliding vortices at intervals $\Delta\bar{t} = 10$ for $0 \leqslant \bar{t} \leqslant 60$. Panels (a)–(g) show the dimensionless reduced gravity, and (h)–(n) show the dimensionless vorticity. Time increases downwards. The Supplemental Material [28] includes an animation of this experiment.

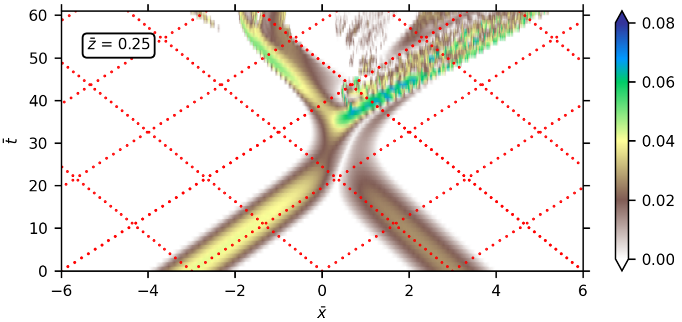

FIG. 11. Hovmöller diagram of the colliding vortices, plotting time against cross sections of dimensionless reduced gravity taken at height $\bar{z} = 0.25$. The red dotted lines indicate the theoretical speed of either vortex individually in an unbounded domain.

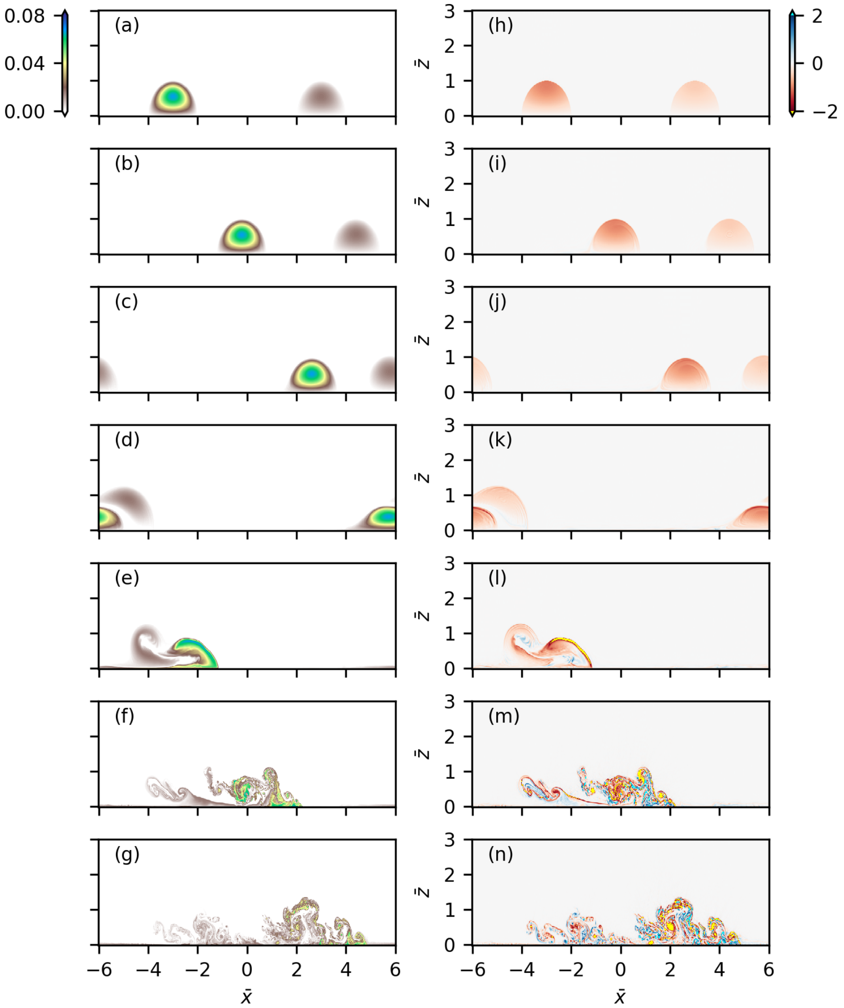

FIG. 12. Plots of the chasing vortices at intervals $\Delta\bar{t} = 20$ for $0 \leqslant \bar{t} \leqslant 120$. Panels (a)–(g) show the dimensionless reduced gravity, and (h)–(n) show the dimensionless vorticity. Time increases downwards. The Supplemental Material [28] includes an animation of this experiment.

$0 \leqslant \bar{z} \leqslant 1.5$, $-6 \leqslant \bar{x} \leqslant 1$ to that in the region $0 \leqslant \bar{z} \leqslant 1.5$, $1 < \bar{x} \leqslant 6$ is 0.31, compared to an initial right-to-left ratio of 0.25.

The corresponding Hovmöller diagram, Fig. 13, indicates a relative slight advance of the stronger vortex front during the encounter. There is some evidence of a reestablished weaker front in the period $80 \leqslant \bar{t} \leqslant 100$, with a corresponding lag compared to its previous trajectory.

VI. CONCLUDING DISCUSSION

A. The isolated vortex

The preceding sections have shown how the stratified dipole of [6] also represents an isolated, negatively buoyant vortex structure traveling along the lower boundary of an otherwise homogeneous, quiescent domain. It may be interpreted as an idealization of a gravity current arising from the release of a finite volume of dense fluid. As with previous idealized modeling of gravity currents,

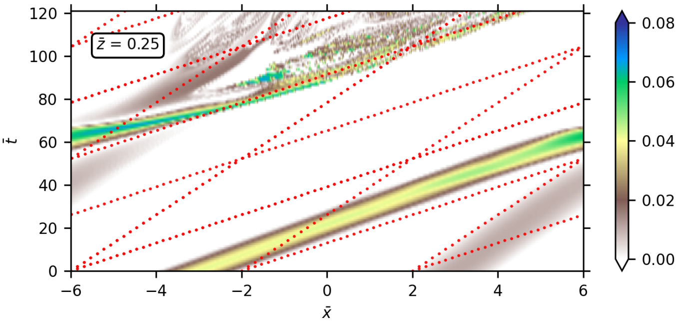

FIG. 13. Hovmöller diagram of the chasing vortices, plotting time against cross sections of dimensionless reduced gravity taken at height $\bar{z} = 0.25$. The red dotted lines indicate the theoretical speed of either vortex individually in an unbounded domain.

differences from an actual quasi-two-dimensional flow include the lack of both surface friction and mixing or diffusion.

It would be difficult to create a balanced distribution of this sort in a laboratory. However, as shown above, it may be realized numerically. Given its apparent stability, one application of this solution would be as a test case for other numerical models. Experimentally, the release of a rotating cylinder of dense fluid could provide a source of buoyancy and vorticity with appropriate bulk values at least. But the lack of a buoyancy-vorticity balance at small scales may lead to some extraneous vorticity creation, mixing, and vortex shedding, which is evident herein for the postcollision phase.

The inflation of the bulk Froude number as $h \to 3.83...$ in Fig. 1 indicates that a buoyancy-vorticity balance gives way to vorticity domination in that limit. Figure 4 shows that the vorticity-stream function distribution becomes more correlated at the same time. This may be compared, for example, with the plots of [14] for experimental vortices similar to the CL dipole. These show a relationship close to 1:1, although with some nonlinearity.

As mentioned at the end of Sec. V B, the vortex created with unbalanced fields, in which the reduced gravity dominates, is more susceptible to breakdown than one in which vorticity dominates. Since significant horizontal buoyancy gradients are usually destabilizing (the balanced vortex in the Bousinesq-Euler framework being an exception), it may be expected that the effects of perturbations to the balanced state are reduced as the buoyancy field becomes relatively weak.

B. Relation to gravity currents

Idealized models of constantly supplied (as opposed to finite-volume) gravity currents often assume discontinuities of density and velocity at the current-ambient interface [3]. The latter condition means the interface is a vortex sheet, and concentration of vorticity in the interface region has been observed in both laboratory experiments and numerical simulations [24,29]. The vortex discussed here has a continuous velocity field across the boundary, although discontinuity in the vorticity field. For much of the parameter range, vorticity is also maximal at or near the boundary (see Fig. 2).

A related issue is the circular boundary of this model, which admits a straightforward analytical solution. It has this shape in common with the CL dipole. However, unlike gravity currents, the experimental flows with which the CL dipole has been compared are observed to be of a similar shape [14]. The postcollision currents herein are arguably more typical of gravity currents, in both shape and vorticity distribution, than is the vortex structure. There has been some work investigating noncircular solutions for dipoles in homogeneous fluids, and on a β plane [30], while enforcing vorticity continuity at the boundary. It could be an interesting avenue of future work to apply these methods to Yih's equation, while relaxing the vorticity condition, to see if vortices could be produced which are more like commonly observed gravity currents in terms of shape and structure.

C. Vortex interactions

For the colliding and chasing vortices, the macroscopic flow features resemble those of nonlinear solitary-wave interactions. The masses of dense fluid recover their velocities after collision, but with an offset in position. The vortices exchange fluid as well as undergoing a significant change in structure compared to their precollision forms, however.

This may be compared with the dipole collisions of [10], which are more shape-preserving in general. There are several points of contrast. The colliding vortices presented here are at an intermediate value of h, for which buoyancy perturbations may be expected to generate small-scale structure. Inasmuch as they are comparable to the CL dipole, the laboratory dipoles do not have an equivalent destabilizing mechanism. The experimental fluid will also have some viscosity, which is neglected in the analysis above but which may stabilize the small scales. Also, the Hydra code is designed to minimize numerical dissipation. Vortex simulations in a different framework may conceivably experience numerical diffusion even without parametrized diffusion, with a similar stabilizing effect.

ACKNOWLEDGMENT

I am very grateful to Prof. David Dritschel for providing the Hydra software and for helpful discussion.

[1] G. G. Rooney, Descent and spread of negatively buoyant thermals, J. Fluid Mech. **780**, 457 (2015).

[2] J. Hacker, P. F. Linden, and S. B. Dalziel, Mixing in lock-release gravity currents, Dyn. Atmos. Oceans **24**, 183 (1996).

[3] P. Linden, Gravity currents—Theory and laboratory experiments, in *Buoyancy-Driven Flows*, edited by E. P. Chassignet, C. Cenedese, and J. Verron (Cambridge University Press, Cambridge, 2012), pp. 13–51.

[4] G. G. Rooney, Similarity-based approximations for the evolution of a gravity current, Q. J. R. Meteorolog. Soc. **144**, 2302 (2018).

[5] R. M. Wakimoto, The life cycle of thunderstorm gust fronts as viewed with Doppler radar and rawinsonde data, Month. Weather Rev. **110**, 1060 (1982).

[6] C.-S. Yih, Vortices and vortex rings of stratified fluids, SIAM J. Appl. Math. **28**, 899 (1975).

[7] J. P. Boyd, Planetary solitary waves, in *Solitary Waves in Fluids*, edited by R. H. J. Grimshaw (WIT Press, Southampton, 2007), pp. 125–158.

[8] S. A. Chaplygin, One case of vortex motion in fluid, Regul. Chaotic Dyn. **12**, 219 (2007).

[9] V. V. Meleshko and G.-J. F. van Heijst, On Chaplygin's investigations of two-dimensional vortex structures in an inviscid fluid, J. Fluid Mech. **272**, 157 (1994).

[10] G.-J. F. van Heijst and J.-B. Flór, Dipole formation and collisions in a stratified fluid, Nature (London) **340**, 212 (1989).

[11] J. S. Turner, *Buoyancy Effects in Fluids* (Cambridge University Press, Cambridge, 1973).

[12] D. G. Dritschel and M. R. Jalali, The validity of two-dimensional models of a rotating shallow fluid layer, J. Fluid Mech. **900**, A33 (2020).

[13] F. Bowman, *Introduction to Bessel Functions* (Dover Publications, New York, 1958).

[14] J.-B. Flór and G.-J. F. van Heijst, An experimental study of dipolar vortex structures in a stratified fluid, J. Fluid Mech. **279**, 101 (1994).

[15] M. Beckers, R. Verzicco, H. J. H. Clercx, and G.-J. F. van Heijst, Dynamics of pancake-like vortices in a stratified fluid: Experiments, model and numerical simulations, J. Fluid Mech. **433**, 1 (2001).

[16] C.-S. Yih, Exact solutions for steady two-dimensional flow of a stratified fluid, J. Fluid Mech. **9**, 161 (1960).

[17] M. E. Stern, Minimal properties of planetary eddies, J. Mar. Res. **33**, 1 (1975).

[18] V. D. Larichev and G. M. Reznik, Two-dimensional solitary Rossby waves, Dok. Acad. Nauk SSSR **231**, 1077 (1976).

[19] J. R. Holton, *An Introduction to Dynamic Meteorology*, 3rd ed. (Academic Press, San Diego, 1992).

[20] G. R. Flierl, Isolated eddy models in geophysics, Annu. Rev. Fluid Mech. **19**, 493 (1987).

[21] D. G. Dritschel, daviddritschel/Hydra, version 1.0.0, Zenodo, https://doi.org/10.5281/zenodo.8416751 (2023).

[22] D. G. Dritschel and J. Fontane, The combined Lagrangian advection method, J. Comput. Phys. **229**, 5408 (2010).

[23] D. G. Dritschel and M. H. P. Ambaum, A contour-advective semi-Lagrangian numerical algorithm for simulating fine-scale conservative dynamical fields, Q. J. R. Meteorolog. Soc. **123**, 1097 (1997).

[24] C. Cafaro and G. G. Rooney, Characteristics of colliding density currents: A numerical and theoretical study, Q. J. R. Meteorolog. Soc. **144**, 1761 (2018).

[25] M. Carr, S. E. King, and D. G. Dritschel, Instability in internal solitary waves with trapped cores, Phys. Fluids **24**, 016601 (2012).

[26] D. G. Dritschel and R. K. Scott, Jet sharpening by turbulent mixing, Philos. Trans. R. Soc. A **369**, 754 (2011).

[27] M. Carr, J. Franklin, S. E. King, P. A. Davies, J. Grue, and D. G. Dritschel, The characteristics of billows generated by internal solitary waves, J. Fluid Mech. **812**, 541 (2017).

[28] See Supplemental Material at http://link.aps.org/supplemental/10.1103/PhysRevFluids.8.123802 for animations of the experiments with colliding and chasing vortices.

[29] L. P. Thomas, S. B. Dalziel, and B. M. Marino, The structure of the head of an inertial gravity current determined by particle-tracking velocimetry, Exp. Fluids **34**, 708 (2003).

[30] T. R. Albrecht, A. R. Elcrat, and K. G. Miller, Steady vortex dipoles with general profile functions, J. Fluid Mech. **670**, 85 (2011).